

Application of Linear Permanent Magnet Flux-Switching Motors to Needle-free Jet Injection

Nick N. L. Do

Auckland Bioengineering Institute

The University of Auckland

70 Symonds Street, Auckland 1010, New Zealand

Email: ldo004@aucklanduni.ac.nz

Andrew J. Taberner and Bryan P. Ruddy

Department of Engineering Science

and Auckland Bioengineering Institute

The University of Auckland

70 Symonds Street, Auckland 1010, New Zealand

Email: a.taberner@auckland.ac.nz; b.ruddy@auckland.ac.nz

Abstract—Needle-free jet injection allows delivery of a liquid drug through the skin in the form of a narrow fluid jet traveling at high speed, minimizing the risks of accidents. Doing this in a controlled way requires an actuator with exceptionally high force density. We propose the use of linear permanent magnet flux-switching motors for this task, and describe their characteristics relative to the needs of jet injection. This paper will introduce a design process which involves the use of artificial neural networks as a means of response surface modelling, combined with non-linear constraint optimization, to deduce a motor design that satisfies all of the challenging linear motor requirements for needle-free jet injection applications.

Index Terms—Drug delivery, design optimization, electromechanical systems, actuators, linear permanent magnet flux switching motor, finite element modelling, ANN, deep learning, machine learning.

I. INTRODUCTION

Needle free jet injection (NFJI) is a safe and efficient method of transdermal drug delivery, which can be realized by forcing a fluid jet between $76\text{ }\mu\text{m}$ and $360\text{ }\mu\text{m}$ in diameter to penetrate the skin at a jet speed (v) typically faster than 100 m/s [1]. Mechanically-powered jet injectors offer limited control over the injection depth and jet velocity, resulting in occasional bruising and other adverse effects [2]. Recently, high force density direct-drive linear motors [3], [4] have been used to enable electronically controlled injectors with superior repeatably and consistency. The voice coil motor (VCM) hand-piece in [5] has a total mass of 426 g , and requires peak electrical power of 5 kW to deliver a $300\text{ }\mu\text{L}$ drug volume. A higher-performance injector based on the tubular permanent magnet linear synchronous motor (PMLSM) assembly in [4] requires 1.4 kW to deliver as much as 1 mL of drug, weighs 322 g for just the coil and magnets, and 600 g in total when adding support components. Even with such progress, this synchronous permanent magnet motor is still larger and heavier than the form factor preferred for a hand-held medical device. In addition, the most efficient and highest force-density implementations of such motors require large amounts of rare-earth permanent magnet material, leading to high cost.

We are therefore motivated to explore alternative motor topologies that could potentially offer both high force density and a reduced cost. One possible alternative is the linear

flux-switching motor (LFSM). Belonging to the the family of doubly-salient permanent magnet motors [6], LFSMs have high thrust density, high tolerance to current overload, lower use of permanent magnet material, and a generally robust construction. They use a passive secondary that can be made out of steel laminations or soft magnetic composite (SMC) to reduce eddy current loss to the minimum. Being able to ignore eddy currents will play an important role in improving the efficiency of design simulation. The amount of permanent magnet (PM) in a LFSM in long stroke applications can be significantly less than that used by a PMLSM[7]. All these advantages are important in bringing a prototype into manufacturing at scale to reach high reliability. However, since the LFSM is still a relatively unexplored topology, the literature has opposing opinions about whether LFSMs outperform PMLSMs [7], [8].

The requirements of direct-drive electric motors for NFJI are demanding: very high pulsed force is required at near stall velocity, but the motor mass must be minimal to ensure the usability of the hand-held injection device. Due the complex flux path in LFSMs and resulting difficulty in semi-analytical modelling for this type of motor, the literature typically makes use of 2D or 3D finite element analysis (FEA) to accurately predict the thrust and cogging force. For modelling accuracy and efficiency advantages, we chose to adopt the tubular variation of LFSM, which can easily be modelled and templated as axisymmetric 2D finite element models (FEM). Traditionally, during the optimization process, each performance valuation requires one FEM evaluation. This means simulation only when needed has poor data re-use, and unpredictable optimization wait time. Instead, we can approach motor design with the response surface method (RSM), by describing the motor performance metrics using empirical equations [9], [10], or using an artificial neural network [11], [12]. In a high order RSM problem with many input variables, large sampling levels for each input are the key to obtaining accurate model predictions. However, for the number of design parameters needed to describe a motor, the time and computation effort required to reach the required sampling levels is high, growing exponentially with the number of parameters.

This study attempts to clarify the performance characteristic of LFSMs, specifically in jet injection applications, by

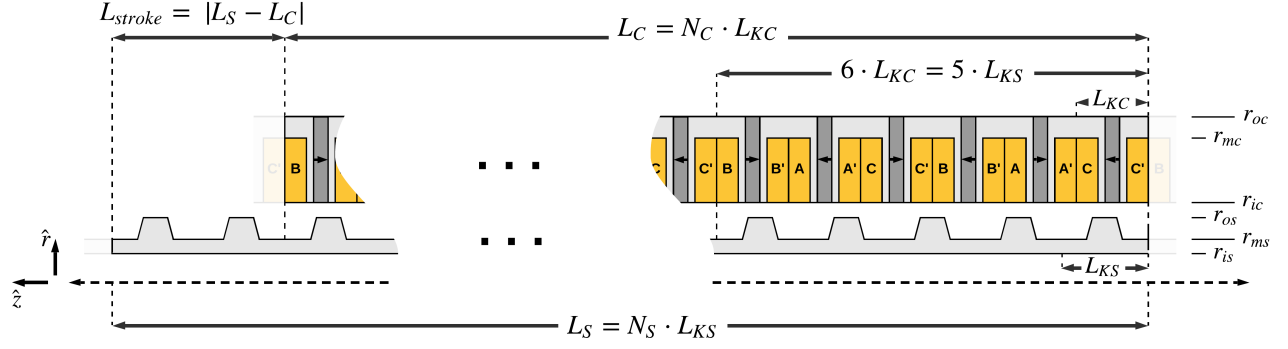
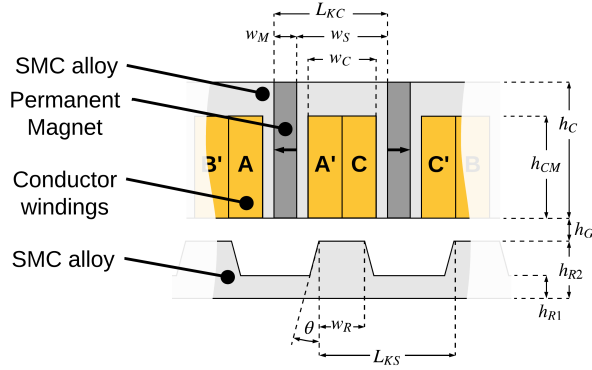
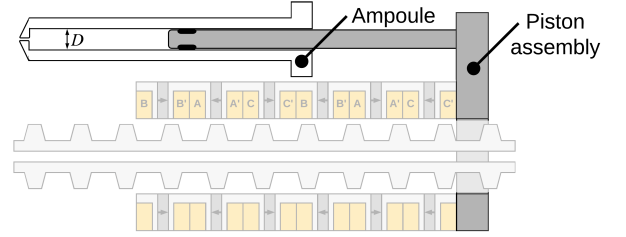


Fig. 1. Schematic of a three-phase tubular linear flux-switching motor (in this case, 6 slot/5 pole). The radii of the SMC track (r_{is} , r_{ms} , r_{os}) and armature (r_{ic} , r_{mc} , r_{oc}) structure are shown. The motor has slot period length L_{KC} , track period length L_{KS} , whole of mover armature length L_C , whole track length or equivalent motor length L_S , length of each overall repeat unit L_{repeat} , and motor stroke length L_{stroke} .



(a) Detailed dimensions



(b) A jet injector driven by a LFSM

Fig. 2. Detailed dimensions of the tubular LFSM: armature assembly widths (w_M , w_S , w_C), armature assembly heights (h_{CM} , h_C), track tooth width (w_R), and track tooth heights (h_{R1} , h_{R2}), tooth angle θ , air gap h_G in (a). A basic schematic of a LFSM driven jet injector and a NFJI drug ampoule with diameter D are shown in (b).

optimizing a LFSM to similar mass and size constraints used in a previous study about a PMLSM [4]. With the help of deep regression ANN, we will develop a topological study and suitable design optimization methodology for LFSMs applied to NFJI in order to achieve this goal.

II. ELECTROMAGNETIC MODEL

A. Structure

We chose to examine a C-core topology, because they typically produce more thrust than E-core topologies [13]. A conventional 6 slot/5 pole LFSM as shown in Fig. 1 has minimal thrust ripple due to cancellation of even order and third order harmonics. However, we chose to study a 6 slot/7 pole LFSM structure because it is reported to also produce more thrust than other configurations, even though it may come at the expense of having more thrust ripple [14].

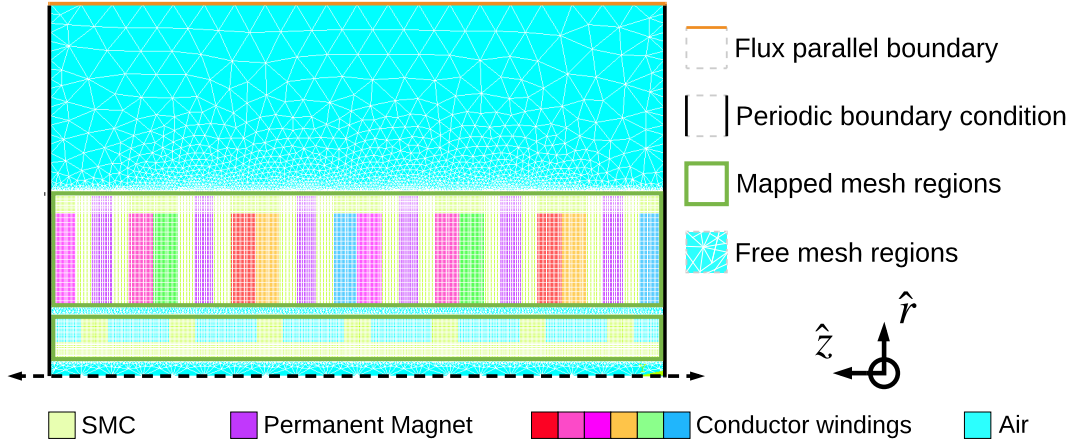
To minimize the moving (and total) mass, the outer sliding armature assembly is selected as the moving element. Each repeating period of the motor consists of 6 axially magnetized permanent magnet rings, 6 SMC cylindrical cores to contain the conductor windings, and 2 circumferentially wound three-phase coil groups. The secondary is passive, and constructed

as an SMC tube with a periodic tooth structure with angled sides. Dimensions are shown for each topology in Fig. 2(a). Fig. 2(b) illustrates how a tubular LFSM can be incorporated in the design of a hand-held jet injector device.

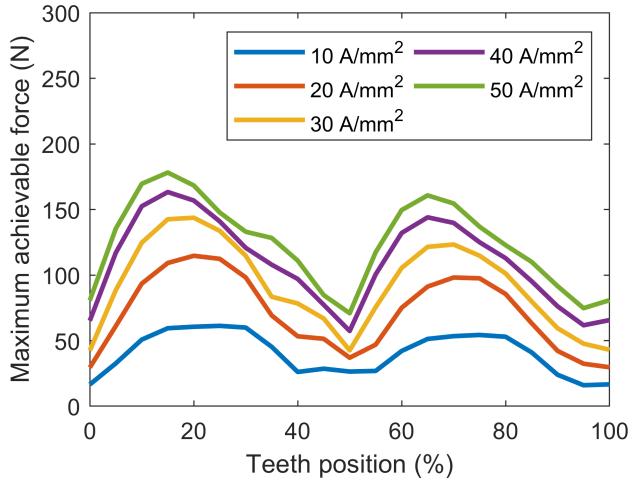
B. Modelling approach

Due to the complex flux pattern inherent to the doubly-salient structure in the mover assembly, estimating average thrust of a design requires knowledge of the maximum achievable forces at different stroke positions.

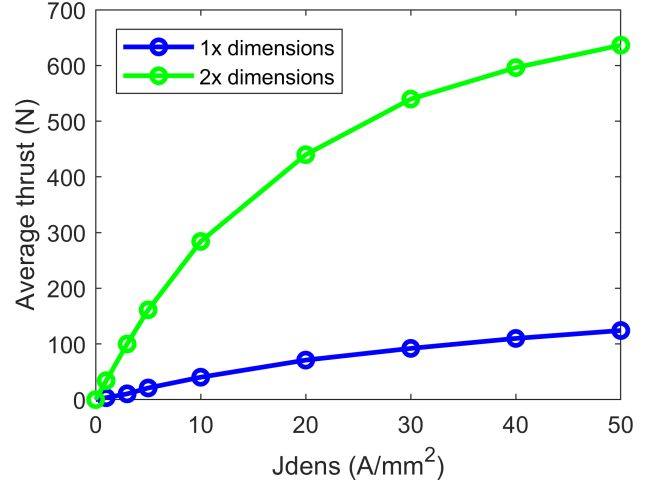
The 6 slot/7 pole machine was modelled in ANSYS MAPDL to measure the force generated on the secondary, as shown in Fig. 3(a). The 2D axisymmetric model implemented in ANSYS 19.2 uses a mapped mesh for the motor parts and a free mesh for the transition regions such as the air gap and the free space surrounding the structure. Periodic boundary conditions were applied at each end of the armature repeat unit along the \hat{z} direction. This setup ignores end effects because later on in the extension to this work, the use of more than one motor repeat period may be considered. The SMC parts and magnets are made out of Sintex SMC prototype materials and K&J Magnetics Grade N45SH, respectively. The



(a) FEA setup, currently $\theta = 0^\circ$



(b) 1x motor: 6 slots, 7 poles, $r_{is} = 2\text{mm}$, $h_{R1} = 2.4\text{mm}$, $h_{R2} = 6\text{mm}$, $r_{ic} = 9.2\text{mm}$, $h_{C1} = 12\text{mm}$, $h_{C2} = 15\text{mm}$, $w_M = 2.7\text{mm}$, $w_S = 10.6\text{mm}$, $w_C = 6.4\text{mm}$, $w_R = 3.4\text{mm}$, $6 \cdot L_{KC} = 7 \cdot L_{KS} = 80\text{mm}$, $\theta = 0^\circ$.



(c) Plot of average thrust for the original motor and another motor with all dimensions doubled ("2x motor") at different current densities: 1, 3, 5, 10, 20, 30, 40, and 50 A/mm²

Fig. 3. The axisymmetric FEA model in ANSYS Mechanical APDL for evaluating force produced on the secondary (a). A plot of maximum achievable force at different track positions for the original motor moving right \rightarrow left (b). A plot that compares the original motor's force production capability to that of a motor twice the size (c).

non-linear B-H relationship of the SMC material is also fully captured in the FEA model. This setup will be crucial to the design optimization process, where many different design configurations need to be tested.

C. Scaling study

There are abundant studies which have explored the effects of changing single design parameters or a few at a time; however, there has not been a study that examine the effect of scaling all LFSM design parameters to benchmark a scaling law. The flux loading created by the permanent magnets pushes the iron structures close to saturation, so we cannot necessarily expect a simple form to the scaling law. The 6 slot/7 pole structure was chosen to be examined first because its tendency to produce larger average thrust at the cost

of higher thrust ripple. An arbitrary 6 slot/7 pole machine and a machine with the same structure but all dimensions doubled ("2x motor") were compared. Fig. 3(b) compares the force production capability at different stroke positions for the original motor. The thrust waveforms are uneven, with high ripple and skewness, which grow as the current density increases. Fortunately, varying the tooth angle to reach a more trapezoidal tooth shape is expected to help reduce the thrust ripple significantly [15].

In doubling the dimensions of a motor, the mass and volume are multiplied by a factor of 8. Hence, when applying the same current density to the coil, the 2x motor will consume 8 times more power. For a permanent magnet motor, one would expect that the force produced would also be eight times higher, in agreement to the motor constant scaling units of

$N/\sqrt{W \cdot kg}$ [16]. The scaling relationship is different in motors operating primarily on the principle of variable reluctance, in which the appropriate normalization for size and power gives units of $N/W \cdot kg$. The scaling difference arises because, in scaling the overall dimensions of the motor by a fixed number, the rates at which PM and winding induction lose effectiveness are different[17]. In a LFSM, the thrust is produced from the flux-switching action of the armature on uni-polar flux produced by the permanent magnet[6], a combination of the two operating principles. These scaling relations apply only up to a certain power level, above which motor performance is impacted by saturation.

The effect of scaling this LFSM is shown in Fig. 3(c). In this particular example, for a current density up to $5 A/mm^2$, the force produced by the 2x motor is indeed 8 times that of the original motor. This ratio drops to 7 times at $10 A/mm^2$ and to below 6 times at $40 A/mm^2$. When optimizing a motor to maximize the motor constant, one should incorporate an extra step to check whether the applied power has not exceeded the scaling relationship implied by the objective of the optimization. Since the extent to which the scaling relationship applies is not well understood in the literature, alternative methods to choosing a good design are to perform a grid search or to use a heuristic method such as a genetic algorithm (GA). The drawback of grid search is computational inefficiency which we can compensate with given a high performance computing facility. On the other hand, GA requires rigorous and heuristic tuning which deviates away from being able to understand how design parameters interact.

III. DESIGN & OPTIMIZATION

From the motor properties study above, we learn that the more saturated the power and average thrust curve becomes, the larger the proportion of thrust fluctuation grows. Our previous effort to optimize PMLSMs for NFJI has involved fixing the length of the motor and the force required to deliver drug at $v = 200 m/s$, while minimizing the required motor mass [4]. A recent study suggests that intra-muscular NFJI can still be realized when the initial peak jet speed of $v_{peak} = 140 m/s$ and subsequent jet speed can be as low as $v = 120 m/s$ [18]. This implies that we can re-frame the problem into finding a LFSM that can produce peak jet speed of $v_{peak} = 140 m/s$ and average jet speed around $v = 120 m/s$. This design goal indirectly lower the required thrust as the result. If no motor could satisfy the thrust requirement, we can gradually relax the mass constraints m until the optimization routine can find a suitable configuration.

In a motor powered NFJI like that shown in Fig. 2(b), ignoring resistance due to fluid viscosity, the actuator force F and jet speed v have the following relation:

$$F = \frac{\pi}{8} \rho v^2 D^2 \quad (1)$$

where ρ is the density of fluid being delivered and D is the diameter of the piston cylinder. We can work backward to find

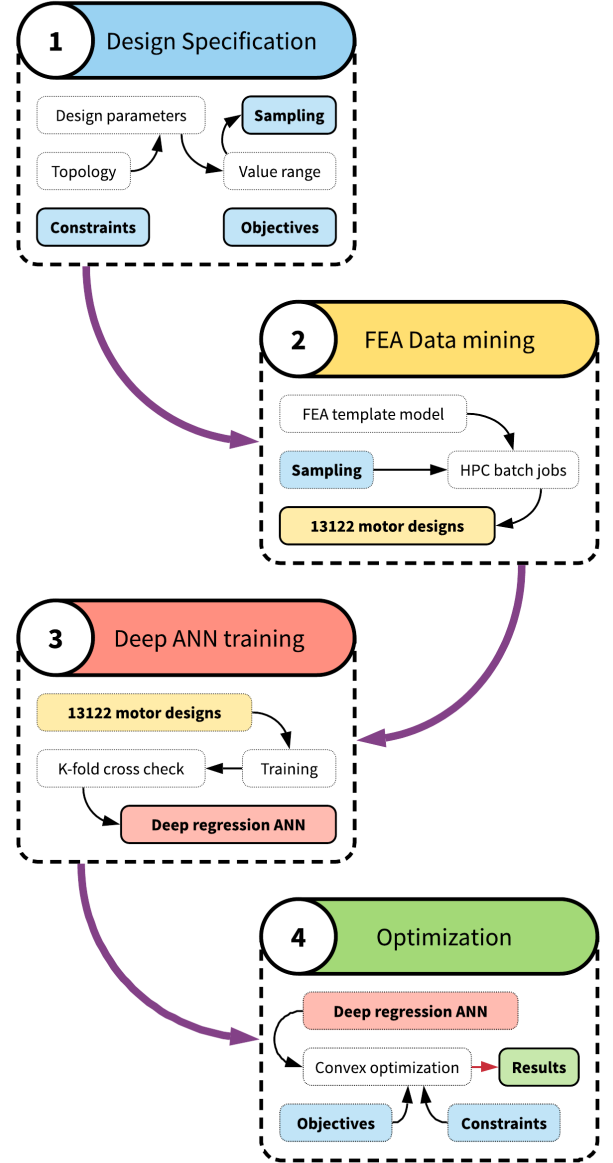


Fig. 4. Flowchart of the motor design process.

the jet speed v when the stroke length L_{stroke} , thrust F , and injection volume V are given:

$$v = \sqrt{\frac{2FL_{stroke}}{\rho V}} \quad (2)$$

In the problem at hand, the injection volume V is fixed to be 1 mL, and maximum achievable thrust F and stroke length L_{stroke} are to be determined. Our optimization goal is to maximize the jet velocity at a given power dissipation to determine an optimized and practical LFSM design to power a hand-held NFJI device. We will first need to obtain sufficient data to train our ANN model by obtaining simulation results from a vast amount of FEM computed on a supercomputer. By

TABLE I
SUMMARY OF MOTOR PARAMETER RANGES

Parameter	Description	Values
α	Ratio of w_M over L_{KC}	0.1 – 0.3
β	Ratio of w_C over w_S	0.7 – 0.9
γ	Ratio of h_{CM} over h_C	0.7 – 0.9
δ	Ratio of w_R or L_{KS}	0.1 – 0.3
ϵ	Ratio of h_{R1} or h_{R2}	0.4 – 0.6
r_{si}	Inner radius of SMC stator core	2 mm
r_{so}	Outer radius of SMC stator core	4 – 10 mm
h_C	Thickness of the mover assembly	10 – 30 mm
h_G	Mover-stator air gap	1.2 mm
L_{repeat}	Length of each 6 slot/7 pole unit	50 – 90 mm
θ	Stator tooth angle	$\arctan(1/2)$

TABLE II
SUMMARY OF MOTOR PARAMETER SAMPLING LEVELS

Params	Level 1	Level 2	Level 3	Unit
α	0.1	0.2	0.3	
β	0.7	0.8	0.9	
γ	0.7	0.8	0.9	
δ	0.1	0.2	0.3	
ϵ	0.4	0.5	0.6	
r_{si}	2.0	-	-	mm
r_{so}	4.0	7.0	10.0	mm
h_C	10.0	20.0	30.0	mm
h_G	1.2	-	-	mm
L_{repeat}	50.0	70.0	90.0	mm
θ	$\arctan 1/2$	-	-	rad

having a big set of data, we can explore the relationship between the motor's geometric parameters and the performance metrics such as the average thrust, maximum thrust, and the cogging force profile. The neural network is then employed in our optimization process to find the desired motor. The entire design and optimization process is summarized in Fig. 4. The rest of this section will describe each step in more details.

A. Specifications & Sampling

The requirements on the final motor design were identified based on the assumption that the motor will be fitted in a hand-held jet injector device, separate from the power source:

- The motor length L_S should not exceed 16 cm and mass M should fall in the range or 300 g to 400 g but not significantly more,
- The average power consumption P_E should be less than 1.6 kW, dictated by the power limit imposed by our battery powered control system in [19].
- The combination of force produced F and stroke length L_{stroke} must allow for 1 mL jet injection through a 200 μm nozzle diameter at an average jet speed of $v = 120$ m/s, and peak jet speed of $v_{peak} = 140$ m/s.

This work investigate and optimize tubular linear 6 slot/7 pole machine with the dimensions presented in Fig. 1 and 2. With consideration to the dimensions and ratios of the desired motor design, the structural design factors and their range are summarized in Table I.

The magnet, conductor and SMC core assembly as a whole body is treated as the mover, and the SMC track with trapezoid teeth is treated as the stator. The stator core inner radius r_{si} and the mover-stator air gap h_G are fixed at 2mm and 1.2mm, respectively. With an effective stator pocket of 4 mm in diameter, the structural support has a place to be added later on. For the ease of manufacturing, there needs to be a reasonable amount of air gap between the stator and mover such as 1.2mm, which comes from our past experience building tubular longitudinal synchronous motor. (Physically, this air gap will include non-magnetic support structures as well as mechanical clearance.) Note that in the data collection process, the motor length L_S

and stroke length L_{stroke} are not yet determined. Instead, the length of each repeat 6 slot/7 pole unit L_{repeat} is iterated upon. To simplify the model the tooth angle θ is set to be the value of $\arctan 1/2$, which makes the width of each tooth extension precisely half the height of the tooth.

Table II shows incremental sampling steps for the structural design factors. From the sampling steps, a design grid of 6561 cases are generated. Additionally, another 6561 cases constructed by input variables created with random values within Table I range were added to help generalize the entire continuous design space better. In total, there were 13 122 independent motor designs to have their average thrust, maximum thrust, and cogging profile predicted by FEA.

B. FEA data mining

Poorly understood physical systems often require FEA for accurate numerical calculation at the cost of long computation time. This work adopts the FEA modelling approach outlined in II-B. The base ANSYS MAPDL 19.2 script was constructed with the intention to allow for easy modification of the input parameters summarized in Table I. For the 13 122 motor designs, we need to determine the cogging force, average thrust, and peak thrust at 1500 W input power. We take force measurements at 20 equally spaced stroke positions and 42 current angle offsets. Since the the mesh of each simulation can be reused for all the different current angle offsets, only the different stroke positions require re-meshing. In total, there are 262 440 input files which represent all the unique permutations of all motor design dimensions, stroke positions, and current angle offsets. Additionally, each input files contain an extra simulation at null applied current to learn about the cogging force at the various stroke positions.

We sent these 262 440 input files to the high performance computing (HPC) infrastructure owned by the New Zealand eScience Infrastructure (NeSI) for execution in parallel batches. Each input file is estimated to take 22 minutes on a two-core Intel CPU with 3 GBs of RAM. Given that the HPC facility allows for any user to execute 1000 jobs in parallel, this consumed 96 228 CPU hours, and took 96 hours to

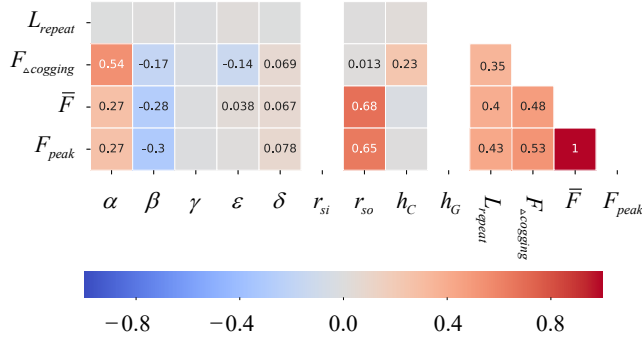


Fig. 5. Heat map which depicts the relationship between different input and output variables of the motor design data set obtained in the FEA data mining step. Red and blue on this scale mean positively and negatively correlated. Small values are hidden.

complete. All verbose output of jobs were collected and doubled checked for errors and warnings, totalling 100.7 GBs of raw data in text format. The necessary information was then reduced back to 13 015 fully captured motor designs in CSV format, demonstrating a very high success rate of more than 99%. The computed thrust output by FEA batches was later further processed and refined into peak to peak cogging force $F_{\Delta cogging}$, average thrust \bar{F} , and peak thrust F_{peak} for use in training the neural network.

One additional advantage of having the data ready ahead of the optimization process is that the available data, though limited, can still provide valuable insights into identifying the principal design parameters. To investigate these hidden relationships, we plot a heat map in Fig. 5. We can learn a number of useful relationships from this heat map:

- α ratio can improve the average and peak thrust at the cost of more peak to peak cogging $F_{\Delta cogging}$,
- r_{so} also improve average and peak thrust without adding more cogging, however, this will inherently add more mass,
- Low β is more preferable,
- Surprisingly, stator tooth design factors such as ϵ and δ has very little influence on the motor performance, even on the peak to peak cogging $F_{\Delta cogging}$

C. Deep regression ANN training

Deep learning belongs to a broader family of machine learning methods and provides the most value in capturing complex non-linear patterns with almost any data set. The data set provides both the continuous input variables (structural design factors), and the continuous output variable (thrust characteristics at a given power), which classify our application as a supervised and regression type of machine learning problem. The ANN model was implemented in Keras and Tensorflow:

- 10 structural parameters and the input power are regarded as the Input layer ($\alpha, \beta, \gamma, \epsilon, \delta, r_{si}, r_{so}, h_C, h_G, L_{repeat}$ and input electrical power P_E),
- 3 performance outputs are regarded as the Output layer ($F_{\Delta cogging}, \bar{F}$, and F_{peak}),

- Adam optimizer is used for ANN training,
- 9 hidden layers of 128 – 256 – 256 – 256 – 256 – 256 – 256 – 128 of densely connected nodes,
- Rectified linear unit (ReLU) activation function is used for the input and hidden layer,
- Linear activation function is used for the output layer
- 75 % and 25 % of the 13 015 data points previously collected are regarded as the training and validation sets, respectively. The split was chosen at random.

After 500 training iterations, the model was shown to have a mean squared error of under 3.7 and mean absolute percentage error of just under 2.89 %. The training and validation errors were similar, showing that the deep regression model is not over-fitted to the training data set.

D. Optimization

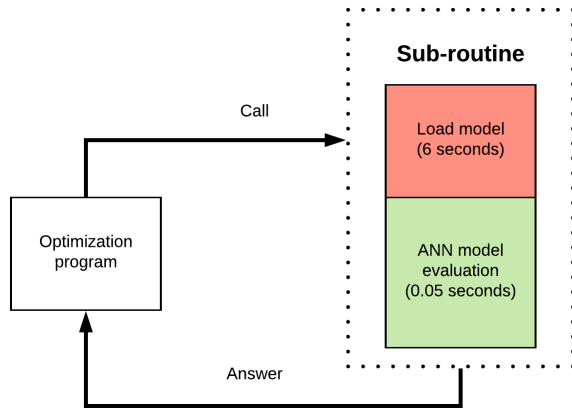
With a fully constructed ANN model of the LFSM within the specified design space, our desired motor was optimized to maximize the normalized jet velocity v to help achieve peak and average jet velocity of 140 m/s and 120 m/s, respectively. The total power P was kept a constant value of 1500 W. The entire optimization search was repeated with different mass constraints m , starting from 350 g.

In this optimization round, there was a single 6 slot/7 pole repeat unit. So far the entire length of the motor L_S has not been chosen yet, because we only looked at grid searching for L_{repeat} . Thus, the overall optimization process was arranged as follows:

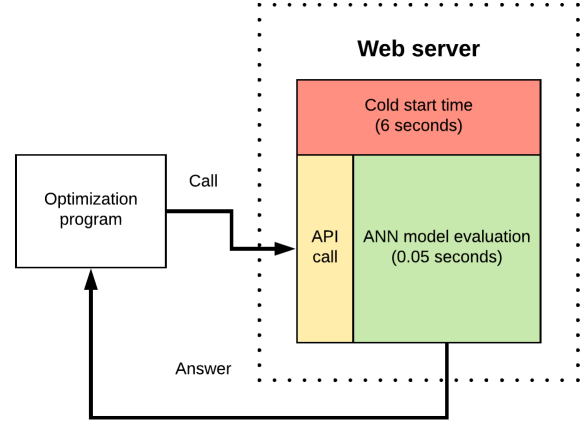
- Limit the search to motors with a total length $L_S = L_{repeat} + L_{stroke}$ in between 120 mm and 160 mm,
- Divide the L_S and L_{stroke} ranges into 41 equally spaced lists each, i.e. [120, 121, 122, ..., 160] mm and [50, 51, 52, ..., 90] mm,
- Create a 2D search zone for each combination of stroke length L_{stroke} and mover length L_{repeat} that makes up a value of L_S , totalling 1681 points,
- Run 1681 inner optimization searches with Matlab constrained convex non-linear optimization function $fmincon()$. Details of the inner optimization will be explained below,
- Plot and identify a motor design that produce the highest average jet speed v at the given mass constraint m .

In more detail, each inner optimization was implemented as follows to complete the 2D search zone for each combination of stroke length L_{stroke} and mover length L_{repeat} :

- Given L_{stroke} in each inner optimization, the values for r_{si} and h_G were taken as fixed; the unknown variables for each search were $\alpha, \beta, \gamma, \epsilon, \delta, r_{so}$, and h_C ,
- The objective function aims to maximize the value of average jet speed v when working backward (equation 2) from the given stroke length L_{stroke} in the previous step, injection volume $V = 1$ mL from the specification, and the average thrust \bar{F} estimated by the ANN model previously constructed and trained,
- The optimization objective function evaluation interacts with the trained ANN model in the fashion of a web

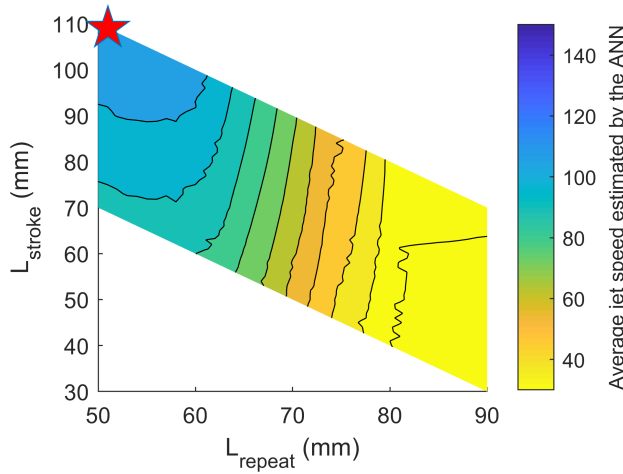


(a) Sub-routine setup: Each objective function evaluation will start a separate sub-routine, taking about 6 seconds.

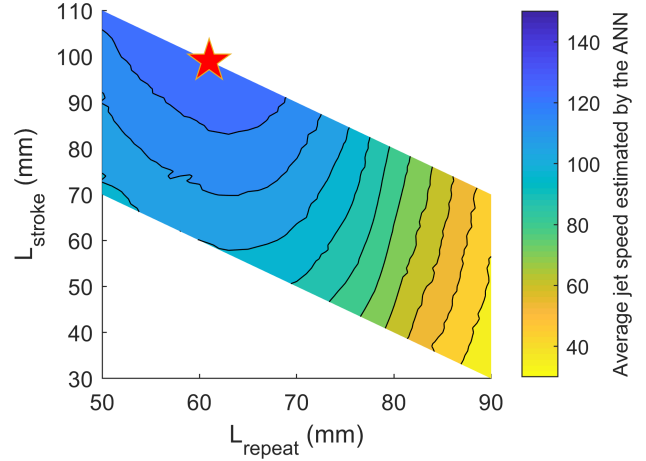


(b) Web-server setup: The model is loaded only once, and all objective function evaluation takes less than 0.05 seconds.

Fig. 6. Two different style of optimization objective function evaluation.



(a) $m = 350$ g: peak average jet speed found is 114.7 m/s



(b) $m = 425$ g: peak average jet speed found is 131.6 m/s

Fig. 7. Mover length $L_{repeat} = [50, 51, 52, \dots, 90]$ mm \times motor length $L_S = [120, 121, 122, \dots, 160]$ mm search map for a motor that produces the highest average injection jet speed v at the lowest (350 g) and highest (425 g) mass constraints. The optimal configurations are highlighted with stars on all subplots. The settings are: injection volume $V = 1$ mL, and input power $P = 1500$ W.

TABLE III
OPTIMIZED MOTOR UNDER DIFFERENT MASS CONSTRAINTS

Mass (g)	α	β	γ	ϵ	δ	r_{si}	r_{so}	h_C	h_G	L_{repeat}	L_{stroke}	\bar{v} (m/s)	v_{peak}	\bar{F} (N)	F_{peak}
350	0.30	0.70	0.71	0.43	0.14	2.00	6.24	10.0	1.20	51	109	114	124	60.42	70.89
375	0.30	0.70	0.90	0.42	0.17	2.00	6.39	10.0	1.20	56	104	120	131	69.50	82.15
400	0.30	0.70	0.90	0.47	0.19	2.00	6.56	10.0	1.20	58	102	127	136	78.79	90.81
425	0.30	0.90	0.90	0.44	0.18	2.00	6.81	10.0	1.20	61	99	132	143	87.43	102.6

server instead of a sub-routine, as illustrated in Fig. 6(b), reducing query time from 6 seconds to just 0.05 seconds,

- The constraint function restricts the motor dimensions so that the entire motor has a mass set by m .

E. Results & discussions

The plots of 2D search maps for $L_{stroke} \times L_{repeat}$ with the highest and lowest mass constraints m are shown in Fig. 7. The optimal motor configurations are highlighted on each plot. As expected, in searches with higher mass constraint values m , the overall average jet speeds were higher. It also appears that

the more difficult the mass constraint, the longer the stroke length L_{stroke} required. More information on all 4 motor configurations is summarized in Table III.

The optimization appears to favor higher values of motor length L_S and stroke length L_{stroke} . The evidence is found in these motor designs where the lengths of the 6 slot/7 pole repeat unit L_{repeat} lean toward the lower limit of 50 mm. This tendency is very similar for both VCMs and LPMSMs [5], [20].

At mass $m = 375\text{g}$, the optimized motor can satisfy the requirement for average jet speed $\bar{v} = 120\text{m/s}$, however the peak jet speed $v_{peak} = 124\text{mm}$ is not satisfactory. The output for mass m of 375 g, and 400 g are also did not meet the specification. Only the optimized motor found at 425 g produce the average jet speed of 132 mm and peak jet speed of 143 mm to satisfy all of the above requirements.

To recall, the LPMSM for NFJI presented in [4] has a base mass of 322 g, base length of 144 mm, and in theory produces peak jet speed of 200 m/s. From the results discussed above, we conclude that for this application, tubular LFSM motors perform worse than LPMSMs. However, the LPMSM uses 200 g of rare earth permanent magnet, but the LFSM only uses 116.5 g of the same material. This demonstrates a significant 42% reduction in high cost rare earth permanent magnet usage.

IV. CONCLUSION

To summarize, we presented an efficient FEA modelling setup for studying tubular LFSMs, a dimensional scaling study on motors of this type, and finally an optimization study for the application of LFSM to NFJI. We also discussed a method of employing an ANN model as a web server to minimize RSM evaluation time. The optimized LFSM for NFJI found was 31% heavier the bench mark LPMSM in [4] but saved 42% in rare earth magnet mass.

Following this work, future work will focus on also gathering 6 slot/5 pole machine data, as well as extending the search ranges of input variables for existing ANN model. The chosen motor design will be further refined to reduce the natural cogging force and thrust ripple using methods which will not compromise the overall force density.

ACKNOWLEDGMENT

The authors would like to thank Mr. Callum Walley for his help with navigating NeSI's High Performance Computing infrastructure, as well as Mr. Yukio Fukuzawa and Mr. Kieran Brennen for their advice with deep learning. This work was supported by the Medical Technologies Centre of Research Excellence, funded by the Tertiary Education Commission of New Zealand.

REFERENCES

- [1] S. Mitragotri, "Current status and future prospects of needle-free liquid jet injectors," *Nature Reviews Drug Discovery*, vol. 5, pp. 543–548, 2006.
- [2] N. C. Hogan, A. J. Taberner, L. A. Jones, and I. W. Hunter, "Needle-free delivery of macromolecules through the skin using controllable jet injectors," *Expert Opinion on Drug Delivery*, vol. 12, no. 10, pp. 1637–1648, 2015.
- [3] A. Taberner, N. C. Hogan, and I. W. Hunter, "Needle-free jet injection using real-time controlled linear Lorentz-force actuators," *Medical Engineering & Physics*, vol. 34, no. 9, pp. 1228–1235, 2012.
- [4] N. N. L. Do, A. J. Taberner, and B. P. Ruddy, "A Linear Permanent Magnet Synchronous Motor for Large Volume Needle-free Jet Injection," *IEEE Transactions on Industry Applications*, vol. 55, no. 2, pp. 1437–1446, 2019.
- [5] B. P. Ruddy, I. W. Hunter, and A. J. Taberner, "Optimal voice coil actuators for needle-free jet injection," in *36th Annual International Conference of the IEEE Engineering in Medicine and Biology Society (EMBC)*, 2014, pp. 2144–2148.
- [6] M. Cheng, W. Hua, J. Zhang, and W. Zhao, "Overview of stator-permanent magnet brushless machines," *IEEE Transactions on Industrial Electronics*, vol. 58, no. 11, pp. 5087–5101, 2011.
- [7] S. R. Aleksandrov, T. T. Overboom, and E. A. Lomonova, "Design Optimization and Performance Comparison of Two Linear Motor Topologies With PM-Less Tracks," *IEEE Transactions on Magnetics*, vol. 54, no. 11, pp. 1–8, 2018.
- [8] J. Wang, W. Wang, K. Atallah, and D. Howe, "Comparative studies of linear permanent magnet motor topologies for active vehicle suspension," in *2008 IEEE Vehicle Power and Propulsion Conference (VPPC)*, 2008.
- [9] D. Hong, B. Woo, D. Koo, and D. Kang, "Optimum Design of Transverse Flux Linear Motor for Weight Reduction and Improvement Thrust Force Using Response Surface Methodology," *IEEE Transactions on Magnetics*, vol. 44, no. 11, pp. 4317–4320, 2008.
- [10] G. Lei, J. G. Zhu, Y. G. Guo, J. F. Hu, W. Xu, and K. R. Shao, "Robust design optimization of PM-SMC motors for six sigma quality manufacturing," *IEEE Transactions on Magnetics*, vol. 49, no. 7, pp. 3953–3956, 2013.
- [11] L. Hadjout, N. Takorabet, R. Ibtouen, and S. Mezani, "Optimization of instantaneous torque shape of PM motors using artificial neural networks based on FE results," *IEEE Transactions on Magnetics*, vol. 42, no. 4, pp. 1283–1286, 2006.
- [12] M. Ashabani, Y. A. R. I. Mohamed, and J. Milimonfared, "Optimum design of tubular permanent-magnet motors for six characteristics improvement by combined taguchineural network approach," *IEEE Transactions on Magnetics*, vol. 46, no. 12, pp. 4092–4100, 2010.
- [13] W. Min, J. T. Chen, Z. Q. Zhu, Y. Zhu, M. Zhang, and G. H. Duan, "Optimization and comparison of novel E-core and C-core linear switched flux PM machines," *IEEE Transactions on Magnetics*, vol. 47, no. 8, pp. 2134–2141, 2011.
- [14] S. L. Chen, K. K. Tan, S. Huang, and C. S. Teo, "Modeling and compensation of ripples and friction in permanent-magnet linear motor using a hysteretic relay," *IEEE/ASME Transactions on Mechatronics*, vol. 15, no. 4, pp. 586–594, 2010.
- [15] J. H. Kim, Y. Li, E. Cetin, and B. Sarlioglu, "Influence of Rotor Tooth Shaping on Cogging Torque of Axial Flux-Switching Permanent Magnet Machine," *IEEE Transactions on Industry Applications*, vol. 55, no. 2, pp. 1290–1298, 2019.
- [16] B. P. Ruddy and I. W. Hunter, "Design and optimization strategies for muscle-like direct-drive linear permanent-magnet motors," *International Journal of Robotics Research*, vol. 30, no. 7, pp. 834–845, 2011.
- [17] J. R. Melcher, *Continuum Electromechanics*. Cambridge, MA: MIT Press, 1981.
- [18] J. W. McKeage, B. P. Ruddy, P. M. Nielsen, and A. J. Taberner, "The effect of jet speed on large volume jet injection," *Journal of Controlled Release*, vol. 280, pp. 51–57, 2018.
- [19] N. N. L. Do, A. J. Taberner, and B. P. Ruddy, "Design of a Portable Pulsed Power System for Needle-free Jet Injection," in *2018 IEEE Energy Conversion Congress and Exposition (ECCE)*, 2018, pp. 6633–6640.
- [20] B. P. Ruddy, J. W. McKeage, R. M. J. Williams, P. M. F. Nielsen, and A. J. Taberner, "A compound ampoule for large-volume controllable jet injection," in *2015 37th Annual International Conference of the IEEE Engineering in Medicine and Biology Society (EMBC)*, 2015, pp. 7341–7344.